The role of molybdenum in the hard-phase grains of (Ti, Mo)(C, N)-Co cermets

Egle Conforto, D Mari, Thierry Cutard

The role of molybdenum in the hard-phase grains of (Ti, Mo)(C, N)–Co cermets

E. Conforto†, D. Mari

Institut de Physique de la Matiére Complexe, Ecole Polytechnique Fédérale de Lausanne, CH-1015 Lausanne, Switzerland

and T. Cutard

Centre de Recherche Outillages, Matériaux et Procédés, Ecole des Mines d'Albi Carmaux, Route de Teillet, 81013 Albi Cedex 09, France

Abstract

The evolution of the core–rim interface in Ti(C, N)-based cermets containing Mo is studied by scanning electron microscopy and conventional and high-resolution transmission electron microscopy as a function of the annealing temperature. A heavily disordered zone on the nanometric scale is observed close to the interface with the core of Ti(C, N) grains in as-sintered samples. It reorders after annealing at a high temperature. This disorder is correlated with the presence of Mo in the rim during sintering, which enhances the strength of the core–rim interface as a barrier for the diffusion of atoms from the core. It avoids the complete dissolution of small Ti(C, N) grains from the original powder and limits the grain growth. It also acts as a barrier against dislocation movements during plastic deformation. This effect, as well as the small final grain size determined by the presence of Mo, contributes to the good mechanical properties of Mo-containing cermets at intermediate temperatures.

§ 1. Introduction

Cermets are materials combining one or more hard phases and a metallic binder as two interpenetrating skeletons (Mari *et al*. 1999). They are mostly used for cutting tools applications at a high speed. In the last few years, Ti(C, N)-based cermets have been widely studied and used (for example Rudy (1976a, b) and Hitachi (1990)). Different metals, such as Ni and Co, are used as the binder phase, in order to combine their high fracture toughness with the good plastic deformation resistance at high temperatures, a property associated with the refractory phase. Ti(C, N)–Co cermets are expected to have the best properties (Cutard *et al*. 1996a).

Ti(C, N)-based cermets are commonly prepared by a powder metallurgy processing route, including a sintering step. Materials with different compositions can be prepared, among which one family is constituted of a mixture of Ti(C, N), Mo_2C, metallic Co and free C (see table 1). Mo_2C is commonly added to facilitate sintering and it is integrated to the cermet final structure. After sintering, the metallic binder is constituted of a fcc Co matrix and contains Mo, Ti, N and C as solute species.

†Author for correspondence. Email: Egle.Conforto@epfl.ch.

The hard-phase grains in the cermet are characterized by a core–rim structure (see figure 1). The core corresponds to the largest original Ti(C, N) powder grains. After dissolution of the smaller grains, the rim grows by reprecipitation of Ti(C, N) around the core. Other elements, such as Mo, can also precipitate during the rim formation, leading to the growth of the (Ti, Mo)(C, N) phase.

In the literature, the growth of the rim around the core is often mentioned as being epitaxial (for example Rolander and Andrén (1988)). The crystalline structure expected for both core and rim is a fcc NaCl-type crystal. Very small differences (Gee *et al*. 1992), if any (for example Heuer *et al*. (1986)), are expected in the crystalline lattice parameters of the rim and the core, even with the incorporation of Mo atoms. These latter are assumed to occupy substitutionally the Ti sites. However, no detailed studies about the role played by the Mo at the core–rim interface on the atomic scale or in the crystallographic structure of the rim are available.

Feusier (1997) and Mari *et al*. (2003a,b) analysed the dependence of the core morphology and rim size with the Mo_2C content. The average grain sizes were 0.90 μm, 0.69 μm and 0.45 μm in samples with low (3 wt%), medium (6 wt%) and high (13 wt%) Mo contents, called TMo3Co6, TMo6Co6 and TMo13Co6 respectively, as listed in table 1 (for a detailed list, see Mari *et al*. (2003a)). In high-Mo-content samples, the core keeps part of its original characteristics, that is small size and sharp edges and corners. The grain size decreases when the Mo content is increased. Mo acts as an inhibitor of the grain growth process, as first observed by Humenik and Parikh (1956). It is likely to slow down the dissolution of the smallest Ti(C, N) powder grains. The physical origin of this effect is, however, a source of controversy (Doi 1986).

The mechanical properties of (Ti, Mo)(C, N)–Co cermets have been studied by Cutard *et al*. (1996b), Feusier (1997) and Mari *et al*. (1999). According to these authors, cermets with different Mo contents show different mechanical behaviours in bending tests, as a function of the temperature. Three domains are observed. At low temperatures ($T < 900^\circ$C), no plasticity is observed in the hard-phase skeleton. It is found that the presence of Mo increases the hardness in the 900–1100°C temperature range and decreases it in the 1100–1200°C temperature range.

The high hardness of high-Mo-content cermets in the 900–1100°C temperature range has been attributed to their small grain size (Mari *et al*. 2003b), on account of the Hall (1951)–Petch (1953) effect. Another origin of the hardening effect of Mo may be the increase in the difficulty of dislocation propagation from the rim to the core, according to Cutard *et al*. (1996a,b).

The aim of this work is to study the Ti(C, N) core–rim interface in presence of Mo at the atomic level, in order to determine the role of Mo atoms in the formation of the rim of the hard-phase grains. The results are then correlated with the mechanical properties.

§ 2. Experimental procedure

In the present work, the basic powder mixture before sintering is constituted of 80.57 vol.% $TiC_{0.7}N_{0.3}$, 13.01 vol.% Mo_2C and 6.42 vol.% Co, corresponding to a high Mo content (TMo13Co6). It was chosen among the different possible chemical compositions for cermets listed in table 1 and is shown in bold. Powders were mixed together, milled with WC–Co balls to obtain a small grain size and good homogeneity. After shaping by uniaxial compaction, samples were sintered at 1450°C for 2 h under an Ar pressure of 30 bar. As-sintered samples were provided

Table 1. Chemical compositions for Ti(C, N)-based cermets, with different Mo_2C contents.

Grade	Amount (vol.%)			Amount (wt.%)		
	$TiC_{0.7}N_{0.3}$	Mo_2C	Co	$TiC_{0.7}N_{0.3}$	Mo_2C	Co
TMo3Co6	90.39	3.21	6.40	84.13	5.30	10.57
TMo6Co6	87.20	6.40	6.40	79.34	10.33	10.33
TMo13Co6	**80.57**	**13.01**	**6.42**	**70.04**	**20.06**	**9.90**

by Stellram-Gland, Switzerland (a unit of Allegheny Teledyne Co., USA). Subsequent anneals were performed at different temperatures for 2 h using a laboratory furnace under a vacuum of 10^{-5} Torr.

The sintered samples were 3.5 mm × 7 mm × 35 mm bars, and the annealed samples 1 mm × 3.5 mm × 35 mm. They were cut into slices by spark cutting and prepared for scanning electron microscopy (SEM) and transmission electron microscopy (TEM) analyses. For SEM observation, squares of about 9 mm^2 were mechanically polished; for TEM, thin foils of 3 mm diameter were manually polished and ion milled.

The scanning electron microscope used in this work was a JEOL JMS-6300F field emission gun, operated at 3–10 kV. The conventional and high-resolution transmission electron microscopy (HRTEM) images, as well as the selected-area electron diffraction patterns (SAED), were obtained with Philips microscopes, EM-430 Twin and CM-300, respectively, operated at 300 kV. Energy-dispersive spectroscopy (EDS) analyses were made with a nanoprobe Hitachi HF-2000 transmission electron microscope, having a probe diameter of 2–5 nm and operated at 200 kV. The electron microscopy software called EMS developed by Stadelmann (1987) for diffraction analysis was used as well as the Digital Micrograph 3.1 software to obtain the Fourier transforms (FTs) of HRTEM images.

During TEM analyses, much attention was paid to the choice of the grains for the core–rim interface analysis in order to avoid the observation of superimposed grains. HRTEM images from the core–rim interface were taken very close to the hole when the absence of superimposed grains was confirmed by the SAED pattern. HRTEM observations were performed on more than ten grains for each sample. As the FT calculations and interplanar distance measurements were obtained from HRTEM images, the crystallographic orientations chosen for HRTEM observations were those involving the largest interplanar distances in a fcc lattice, that is the [001], [011] and [111] zone axes. Through this systematic procedure the evolutions of the core–rim interfaces as a function of the annealing temperature were followed in different samples.

§ 3. Results

3.1. *Morphology of as-sintered and annealed samples*

Figure 1 shows general views of polished TMo13Co6 samples in SEM secondary-electron images. Figure 1 (a) corresponds to an as-sintered sample, while figure 1 (b) shows a sample annealed at 900°C for 2 h. In both cases, the typical core–rim structure of cermets is clearly observed. No differences are observed in the hard-phase grain size after annealing, and the average size remains close to 0.5 μm. The core and the rim are identified by their contrast: the core is darker, surrounded by the rim that is lighter. The signal is higher in the rim because its average atomic

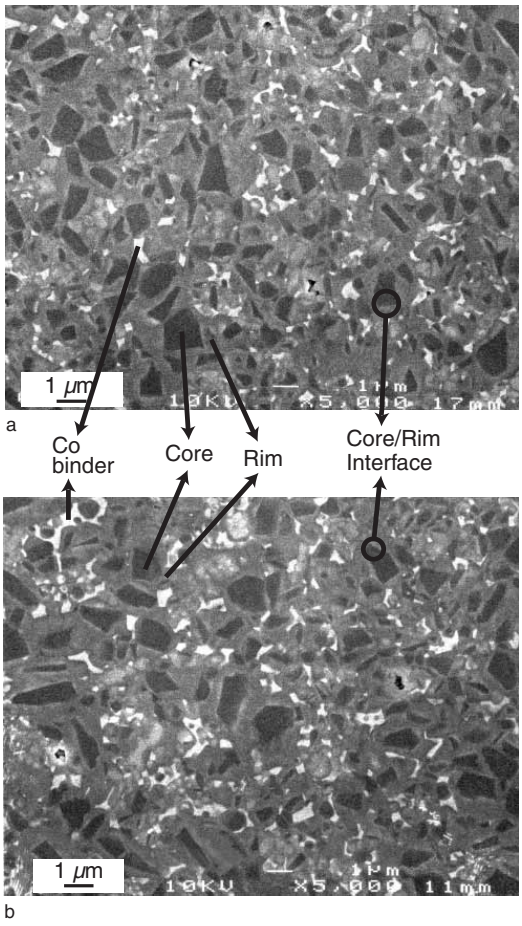

Figure 1. SEM general-view images of polished TMo13Co6 samples showing the cermet microstructure, namely core, rim, core–rim interfaces and the Co binder, for (a) an as-sintered sample and (b) a sample annealed at 900°C for 2 h.

number Z is higher (it contains Mo, with $Z = 42$) than that of the core, which is constituted of pure $TiC_{0.7}N_{0.3}$ (van Essen 1979). In fact, even if the secondary-electron signal is a mixture of chemical and topographical contributions, the main information from our images is chemical, because the topography was strongly flattened by polishing. The Co binder skeleton, which is continuous in three dimensions, is bright. This latter is found to be of a single-crystal nature with fcc structure over several tens of square micrometres as observed in dark-field TEM images, in agreement with previous works (Heuer *et al*. 1986).

3.2. *The Mo distribution*

Some EDS analyses were performed on as-sintered and on annealed samples in order to map the Mo distribution inside the (Ti, Mo)(C, N) grains and, in particular, at the core–rim interface. The distribution of other metallic atoms such as Ti and W was also mapped. As the sensitivity of the EDS technique is low for light elements, such as C and N, their profiles are not shown.

Figure 2 (a) shows a TEM image of a typical grain where an EDS line scan, formed by eight aligned EDS analysis points, is indicated. The distance between two data points is 60 nm except between points 5 and 6. Point 5 is placed 20 nm from the interface in the rim phase and point 6, 20 nm from the interface in the core phase.

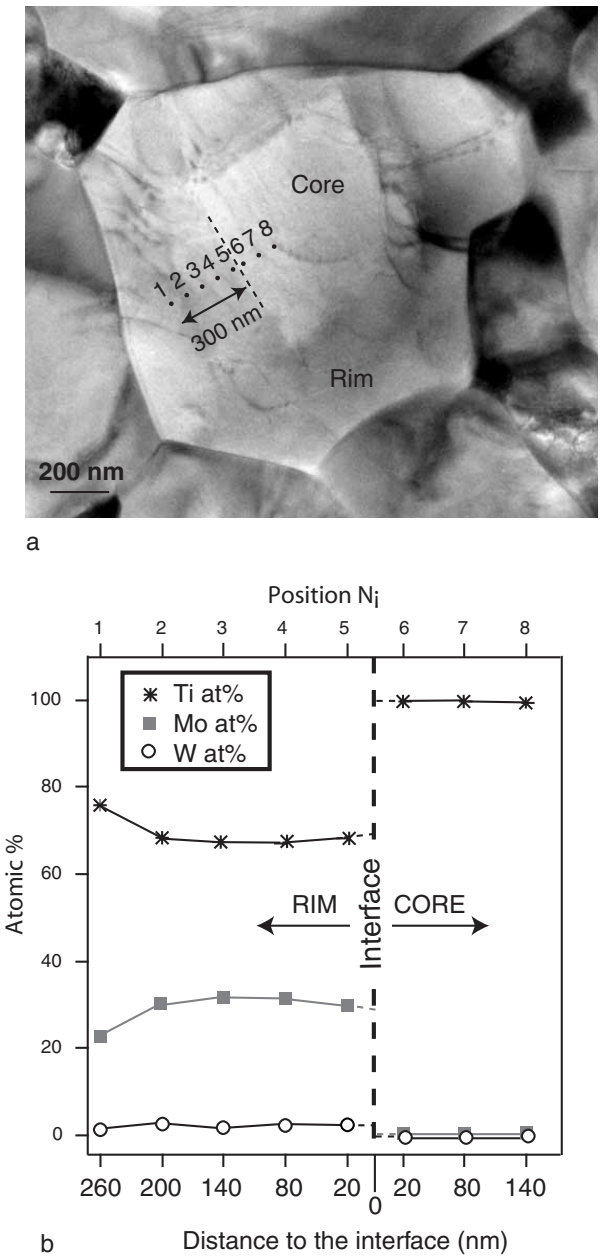

Figure 2. (a) TEM image of one cermet grain where an EDS line scan, formed by eight aligned EDS analysis points, is indicated; (b) graph showing the evolutions of the atomic percentages of Ti, Mo and W as functions of the distance to the interface, in both the rim and the core.

Figure 2 (b) shows the corresponding evolutions of the atomic percentages of Ti, Mo and W as functions of the distance to the interface, from the rim towards the core. Some W is detected in the rim close to the interface with the core, as an impurity coming from the WC balls used to mill the base powder mixture. Both Ti and Mo atoms are present in the whole analysed region, but the respective evolutions of their atomic concentrations as functions of the distance to the interface are opposite. The Mo atoms are highly concentrated close to the core interface (within a distance of about 100–150 nm), and their concentration decreases towards the grain boundary. Ti atoms, which are present in more than 80% of metallic sites far from the interface (at distances larger than 150 nm), are partially substituted by Mo atoms close to the interface. On the core side, only Ti was detected, without

any Mo or W. These latter do not diffuse into the core that remains unchanged after sintering as well as after further annealing. The analyses shown above correspond to one typical annealed sample, but the results are very similar for as-sintered samples.

3.3. *Interface analyses*

3.3.1. *As-sintered samples*

Figure 3 (a) shows a low-magnification TEM image of an as-sintered core–rim-type grain. The contrast is the opposite of that shown in the SEM image: the core is lighter and the rim is darker. This difference occurs because the rim contains Mo that is less transparent to transmitted electrons than the elements present in the core. Some dislocations are seen in the rim and in the neighbouring grain, created by plastic deformation during cooling after sintering. Such defects are often observed

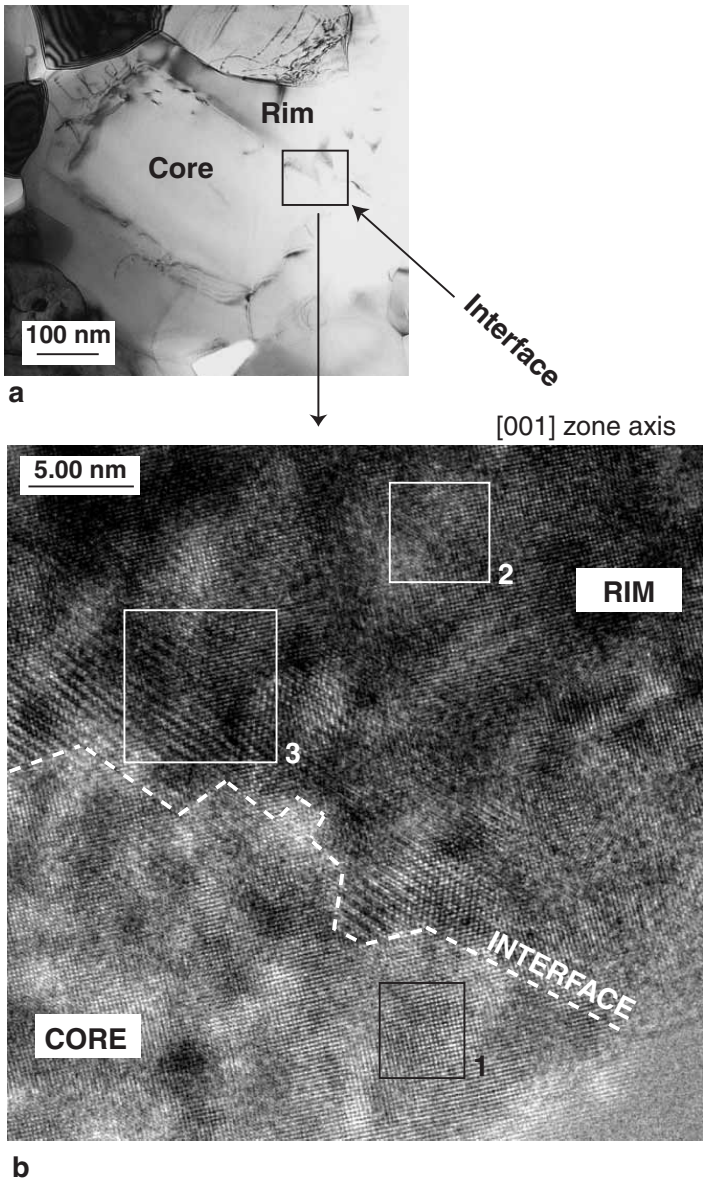

Figure 3. TEM images showing a core–rim grain of an as-sintered sample: (a) in low magnification; (b) detail of (a) showing the core–rim interface along the [001] zone axis. Regions labelled 1, 2 and 3 are examined in detail in figure 4.

on a submicrometric scale. They are hereafter called submicrometric dislocations. It is important to note that their density is lower in the core than in the rim, which denotes that it is difficult for them to cross the interface.

In figure 3 (b), which is a detail of figure 3 (a), the core–rim interface (indicated by the white broken line) can be seen in the [001] zone axis. It can be observed that the core, at the interface with the rim, has kept sharp edges and corners after sintering in presence of the high Mo content, in agreement with the work of Feusier (1997). The crystal on the core side is almost perfectly oriented along a [100] zone axis. On the rim side, on the contrary, the crystal is constituted of small areas a few nanometres in size, with some of these oriented parallel to the core, and others slightly misoriented with respect to the first. When the distance to the interface increases, perturbations progressively disappear and one can find again the epitaxial lattice structure and orientation. In the rim close to the interface with the core, moiré fringes can be observed, indicating that the two superimposed crystals (core and rim) are not exactly identical. In fact, the presence of moiré fringes suggests that the core–rim interface is not vertical, but inclined (see also figure 6). The white broken line indicates the position of the interface at the top of the foil. The other intersection corresponds to the extension limit of moiré fringes (15–20 nm) on the rim side.

Three different regions in figure 3 (b) (labelled 1, 2 and 3) are considered for analyses in detail of these characteristic features. Region 1 is located close to the core–rim interface in the core phase, and region 3 is close to the core–rim interface (distance $r < 15$ nm) in the rim phase. Region 2 corresponds to the 15 nm $< r <$ 50 nm range from the interface in the rim.

In figure 4, regions 1, 2 and 3 from figure 3 (b) have been enlarged. The FTs corresponding to each region are also shown. In the HRTEM image of the core (figure 4 (a)), atomic columns are perfectly aligned along the [001] direction of the fcc zone axis. Identical crystallographic information is provided by the SAED pattern and by the FT that exhibits sharp spots. In the rim (figure 4 (b), region 2), regions oriented parallel to the core are observed, as at the lower right, simultaneously to slightly misoriented regions (as at the upper left of the HRTEM image in figure 4 (b), labelled MNR) where only $(2\,\bar{2}\,0)$ dense planes are visible, which denotes a rotation around the $[1\,\bar{1}\,0]$ axis. The edges of dense planes may contain edge dislocations with $\frac{1}{2}\langle 110\rangle$ Burgers vectors, as indicated by white arrows. A grazing view of the same area (figure 5) shows more evidently such dislocations. Since, at a lower magnification, these dislocations are not observed in bright-field conditions, they may be part of very small prismatic dislocation loops surrounding clusters of interstitial atoms. They are hereafter called nanosize dislocations, to differentiate them from the submicrometric dislocations described before. The FT corresponding to the HRTEM image in figure 4 (b) is less sharp than that of the core. The supplementary spot D is an effect of the local lattice misorientation. In the Inverse Fourier Transforms (IFTs) in figure 4 (b) we observe that the direction of the planes at the origin of spot D coincides with that of the (220) planes of Ti(C, N) and the spacing, with that of (200) planes of Ti(C, N). This will be discussed below with reference to figure 4 (c).

The slightly misoriented nanoregions, present in region 2, are more concentrated in region 3 (figure 4 (c)). The FT obtained from this region is very fuzzy. The spots close to the centre, labelled M, denote a large periodicity. They are associated with the moiré fringes. Their direction and spacing are observed through its IFT. The

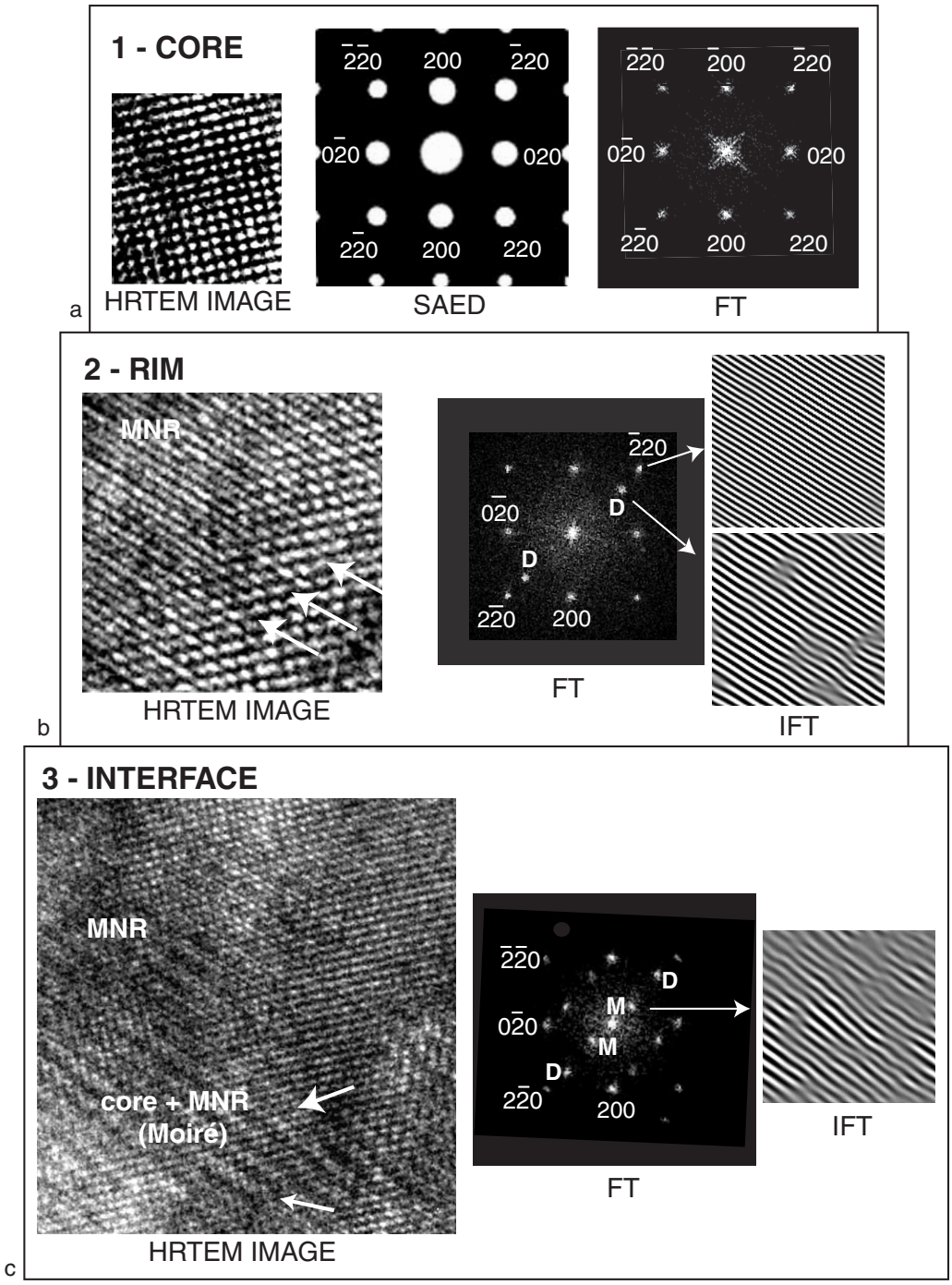

Figure 4. HRTEM image of regions labelled 1, 2 and 3 in figure 3 (b), and their corresponding FTs. Misoriented nanoregions are labelled MNR. (a) The core (region 1), and its corresponding SAED pattern, which contains the same information as its FT. (b) The rim (region 2 corresponding to the 15–50 nm range from the interface) shows two nanoregions, the first oriented parallel to the core (at the bottom right) and the second, rotated by 45°, respectively, to the first (at the top left). The supplementary spot D is an effect of the lattice misorientation, as shown by the IFT. (c) The rim at the interface with the core (region 3 corresponding to the 0–15 nm range) shows dislocations (indicated by white arrows) and moiré fringes (supplementary spot M in the FT), these latter resulting from the superposition of the core and the misoriented nanoregion lattices.

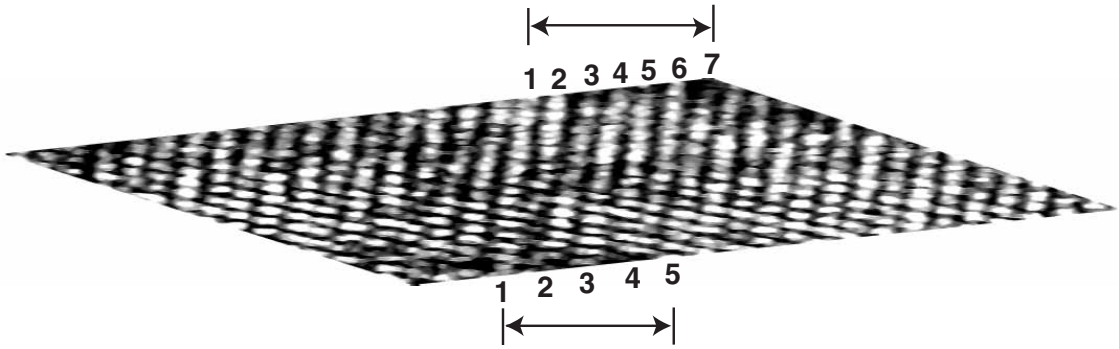

Figure 5. HRTEM image from figure 4(b) in a small-angle view. The lattice distortion is clearly visible between the bottom (parallel to the core) and the upper part (a misoriented nanoregion), with a difference in periodicity of $\frac{7}{5}$ times.

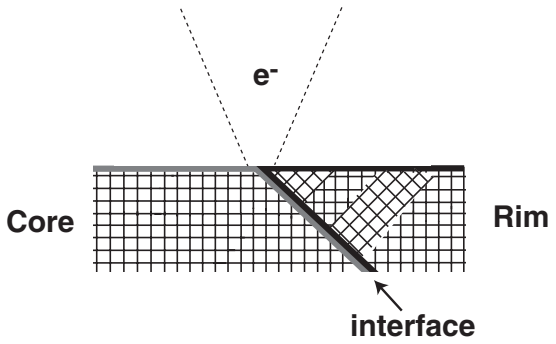

Figure 6. Cross-sectional schematic representation of the superposition between the core lattice and that of a 45°-rotated nanoregion in the rim, corresponding to the moiré fringes of the HRTEM image in figure 4(c).

deconvolution indicates that they result from the superposition of the Ti(C, N)(220) atomic planes from the core lattice and the Ti(C, N)(200) atomic planes of a misoriented nanoregion in the rim (at the origin of spot D). This latter is rotated by 45° with respect to the core orientation, around the [001] direction. The schematic representation of this superposition at the interface with respect to the electron beam is shown in figure 6.

An average increase in the interplanar distances in the rim lattice with respect to that of the core is also observed, in good agreement with the observations by Gee *et al.* (1992). For the core lattice, the interplanar distances measured are those expected for $TiC_{0.7}N_{0.3}$ (Aigner *et al.* 1994). This increase is mainly perceptible in the vicinity of the core interface ($0\,\text{nm} < r < 20\,\text{nm}$), and directly measurable on HRTEM images obtained in [001] and in [110] zone axes. Table 2 shows a list of the average interplanar distances measured over a large number of HRTEM images for the core that shows the expected parameters for the fcc Ti(C, N) and for the rim, for the same crystallographic directions. For each direction, the increase in the rim is, on average, about 3%. The corresponding increase in the cell volume is about 10% with respect to that of the core.

Occasionally, some nanoregions can also show locally reduced interplanar distances with respect to the Ti(C, N). For instance, a local value $d_{020} = 0.212 \pm 0.004\,\text{nm}$ was measured. The extension in the rim from the interface in which the lattice is deformed corresponds to that in which the Mo concentration is high

Table 2. Average interplanar distances measured on HRTEM images, lattice parameters a and cell volumes V_{cell} for the core (expected values for the fcc Ti(C, N) structure) and for the rim in as-sintered samples.

	Interplanar distance (nm)			a (nm)	V_{cell} (10^{-3} nm^3)
	d_{111}	d_{200}	d_{220}		
In the core	(0.247 ± 0.003)	(0.215 ± 0.003)	(0.152 ± 0.002)	0.430 ± 0.003	(79.51 ± 0.01)
In the rim ($0\,\text{nm} < r < 20\,\text{nm}$)	(0.255 ± 0.004)	(0.222 ± 0.004)	(0.157 ± 0.003)	0.444 ± 0.004	(87.53 ± 0.01)

($0\,\text{nm} < r < 100\,\text{nm}$). Far from the interface ($r > 100\,\text{nm}$), the interplanar distances in the rim tend to those of the core.

3.3.2. *Annealed samples*

Figure 7 (a) shows a core–rim-type grain in a sample annealed at 900°C for 2 h, where submicrometric dislocations are still visible. Figures 7 (b) and 7 (c) are details of the core–rim interface of the grain in figure 7 (a), oriented in the [001] and [011] zone axes, respectively. From both of these it can be observed that the sharp edges and corners of the core at the interface with the rim are kept unchanged even after annealing. In figure 7 (b), the core exhibits atomic columns perfectly aligned along the [001] direction of the fcc zone axis and the corresponding Fourier transform exhibits sharp spots. The disorder is still observed in the rim close to the interface with the core ($0\,\text{nm} < r < 10\,\text{nm}$), but less pronounced than in the corresponding zones of the as-sintered sample. In inset 2, on the right, $(\bar{2}20)$ planes of a small zone, rotated around the $[\bar{1}10]$ direction, are indicated by a white arrow, but they are weakly perceptible in the image. The corresponding supplementary spots D are accordingly hardly visible in the FT, which is, on the whole, less sharp than that obtained from the core. The same observations are made when examining the interface through the [110] zone axis (figure 7 (c)).

The difference between the average interplanar distances of the core and rim also decreases after annealing. The comparative values are given in table 3. The region where these differences are still perceptible is now confined to the immediate vicinity of the core interface ($0\,\text{nm} < r < 10\,\text{nm}$). The difference in each direction is, on average, 1.4%, as against 3% in as-sintered samples. The difference in cell volume between core and rim accordingly changes from 10% in as-sintered samples to 4% after annealing at 900°C for 2 h.

In figure 8, TEM images correspond to a sample annealed at 1150°C for 2 h. In figure 8 (a) we can see the whole grain. Figures 8 (b) and (c) are details of the figure 8 (a) showing the core–rim interface oriented along [001] and [011] zone axes respectively. The sharp edges and angles of the core appear unchanged at the rim interface. In figure 8 (b), both core and rim show atomic columns well aligned along the [001] direction of the fcc zone axis. The FT of the core is always sharp as in as-sintered samples, which proves that the core does not change upon annealing. In the rim close to the interface (inset 2), the disorder in the lattice is hardly visible. The same results are obtained from observations through the [110] zone axis (figure 8 (c)). A very slight residual misorientation of the rim with respect to the core is observed, which makes the (111) planes less visible, as shown in inset 4. This very slight misorientation concerns a large area in the rim close to the interface, and nano-

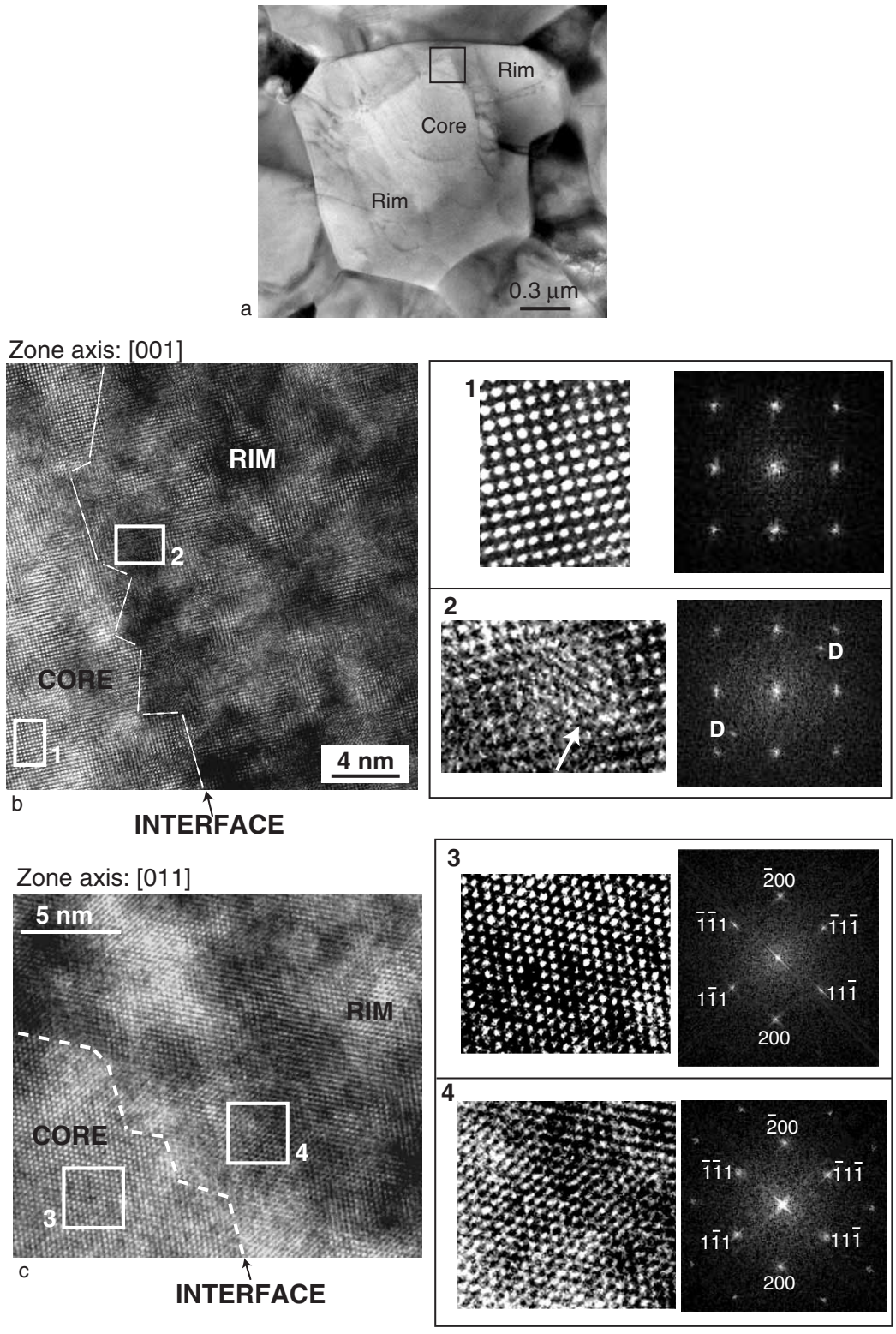

Figure 7. (a) Low-magnification TEM image showing a core–rim-type grain of a sample annealed at 900°C for 2 h; (b) on the left, the core–rim interface in the [001] zone axis and, on the right, inset 1 showing the details and inset 2 showing the rim details in the 0–10 nm range from the interface, and their corresponding FTs; (c) the same as (b) for the [011] zone axis.

Table 3. Average interplanar distances measured on HRTEM images, lattice parameters a and cell volumes V_{cell} for the core (expected values for the fcc Ti(C, N) structure) and for the rim in samples annealed at 900°C for 2 h.

	Interplanar distances (nm)		a (nm)	V_{cell} (10^{-3} nm^3)
	d_{111}	d_{200}		
In the core	(0.247 ± 0.003)	(0.215 ± 0.002)	0.430 ± 0.003	79.51 ± 0.01
In the rim ($0\,\text{nm} < r < 10\,\text{nm}$)	(0.250 ± 0.004)	(0.218 ± 0.003)	0.436 ± 0.004	82.88

regions are no longer observed. Also, neither differences in interplanar distances between core and rim ($r > 10$ nm) nor in cell volumes are now observed.

§ 4. Discussion

The present results show that the rim growth around the core, although tending to reproduce the core lattice, is not fully epitaxial. It is influenced by the presence of Mo atoms that precipitate around Ti(C, N) cores and form a (Ti, Mo)(C, N) layer (the inner rim). The effect of Mo can be observed in as-sintered samples through the presence of crystallographic disorder at the nanometric level and through the increase in the cell volume.

The nanometric defects are confined to the region in the inner rim where the Mo concentration is high. They are observed after sintering at 1450°C but progressively disappear after successive anneals at 900 and 1150°C for 2 h (figures 9 (a) and (b) respectively), when the reordering is complete. This evolution cannot be ascribed to the possible diffusion and redistribution of Mo atoms in the rim volume over large distances after annealing, because the activation energy for the diffusion of heavy elements in Ti(C, N) is higher than 5 eV (Kosolapova 1990). Indeed, the diffusion coefficient of Mo is of the order of $D = a^2 \nu_D \exp(-E/kT)$, where a is the lattice parameter, ν_D is the Debye vibration frequency ($\nu_D = 10^{13}\,\text{s}^{-1}$ and $a^2\nu_D \approx 10^{12}\,\text{nm}^2\,\text{s}^{-1}$) and $E = 5$ eV. Then, the corresponding diffusion distance during the time t is $X = (tD)^{1/2}$ (Einstein formula). In order to have a significant diffusion over a distance $X = 400$ nm (the order of the rim thickness) during time $t = 7200$ s, the temperature must be about 2500 K, thus much higher than those at which our anneals were performed. The Mo concentration is accordingly expected to remain constant in the inner rim even after annealing. These observations indicate that reordering may occur by short-range diffusion.

The observation of defects such as dislocations in the core–rim grain has been reported in the literature. Some authors attributed the presence of submicrometric dislocations distributed in the core and in the rim either to the thermal expansion mismatch between core and rim (Heuer *et al.* 1986) or to the accommodation of the lattice mismatch observed between them (Gee *et al.* 1992). Our observations cannot be interpreted in the frame of these hypotheses only. The defects that we observed are indeed of two different orders of magnitude in size (nanometric defects and submicrometric dislocations). Moreover, they have different spatial distribution in the core–rim grain and do not show the same behaviours as functions of the annealing temperature. They accordingly have two different origins. On the one hand, long, submicrometric dislocations are observed in as-sintered samples over the rim volume (figure 3 (a)). Since these dislocations appear in the hard-phase grains

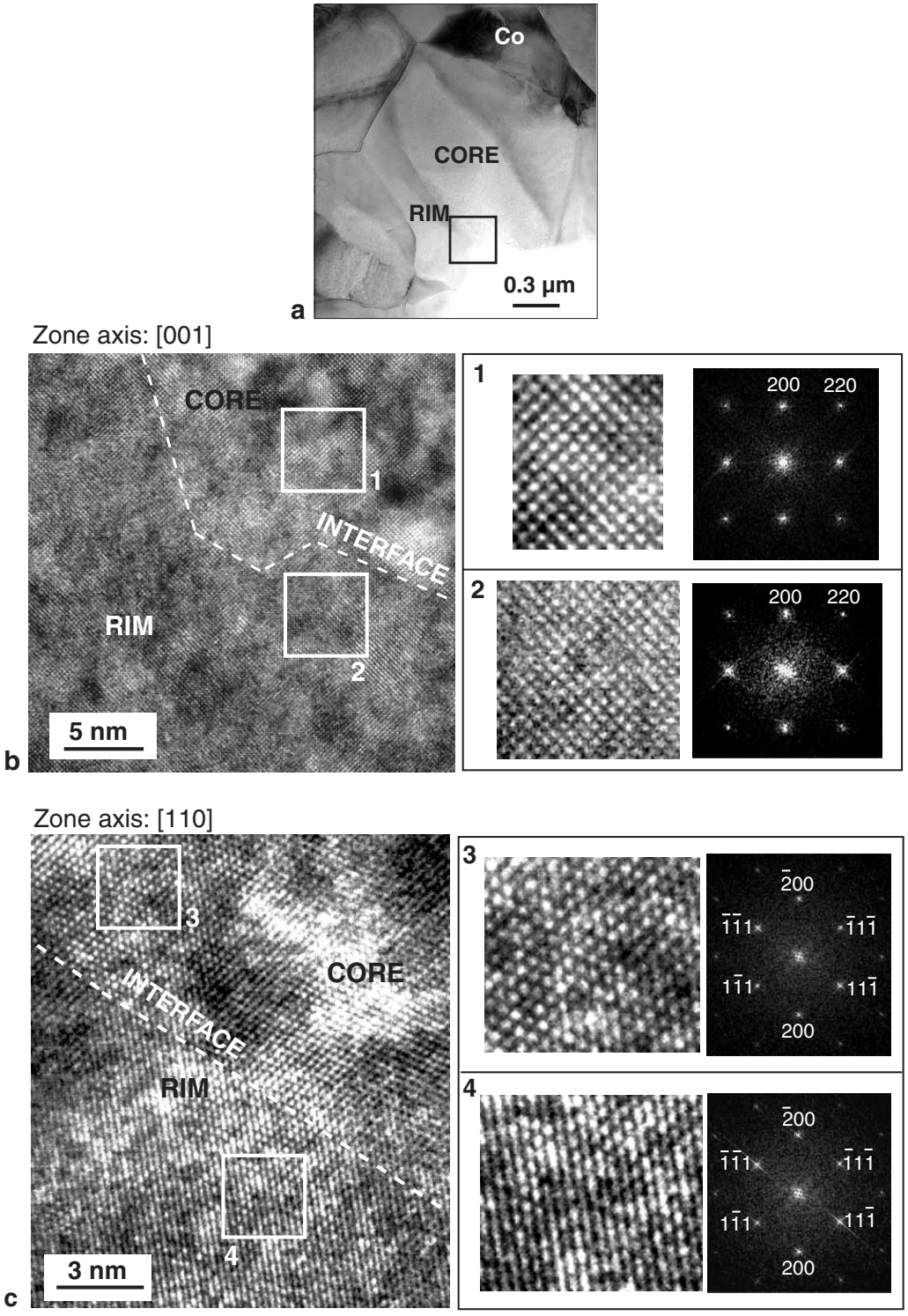

Figure 8. (a) Low-magnification TEM image showing a core–rim-type grain of a sample annealed at 1150°C for 2 h; (b) on the left, the core–rim interface on the [001] zone axis and, on the right, inset 1 showing the core details and inset 2 showing the rim details in the 0–10 nm range from the interface, and their corresponding FTs; (c) the same as (b) for the [011] zone axis.

during cooling, their nucleation is attributed to thermal stress, in agreement with the work of Heuer *et al*. (1986). On the other hand, nanosize defects observed after sintering in the inner rim close to the core–rim interface cannot result from thermal stresses. In that case, the disorder would indeed be observed after an anneal at

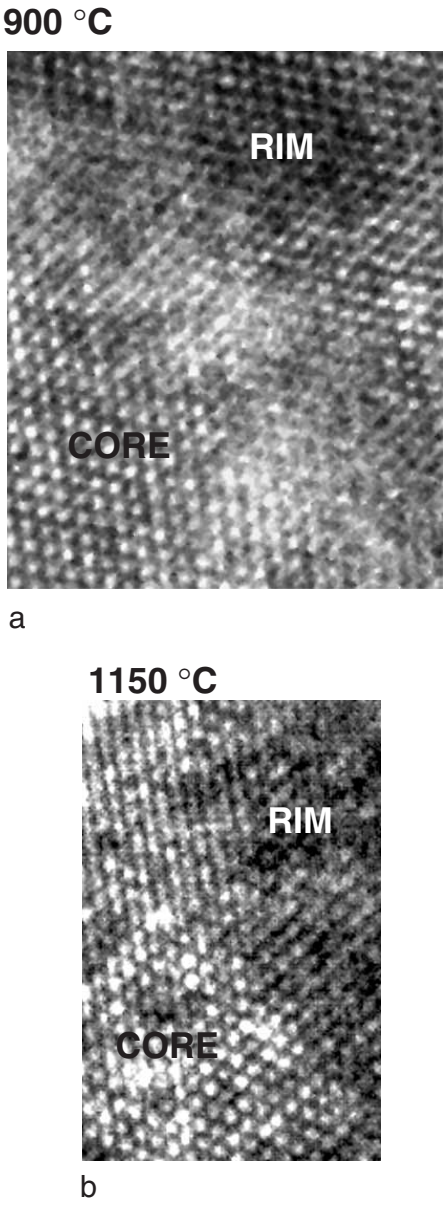

Figure 9. HRTEM images of the core–rim interface showing the increase in the crystallographic order in samples annealed for 2 h at: (a) 900°C and (b) 1150°C.

1150°C as well, because thermal stress is also created during cooling after annealing at this temperature.

Some studies have demonstrated the influence of Mo atoms in the formation of the (Ti, Mo)(C, N) inner rim during the first step of the sintering process. According to those studies, in the early stage of sintering the smallest grains, which have a high surface-to-volume ratio, are dissolved and the Mo-rich inner rim grows around the largest original Ti(C, N) grains (Doi 1986, Zackrisson *et al.* 2001). These authors proposed that the dissolved Ti, C, N and Mo atoms are transported by the Co binder, and the inner rim grows before the sintering temperature is reached. As soon as it forms, the inner rim acts as an efficient barrier against further core dissolution, which allows the largest cores to keep their original sharp angles and edges. The inner rim is subsequently covered by the outer rim, which contains less Mo and grows by reprecipitation during sintering, in the presence of a liquid phase. This description accounts for, firstly, the reduced grain growth of high-Mo cermets with

respect to low-Mo cermets and, secondly, the sharp edges and corners at the core–rim interface.

During the inner rim formation, some disorder is probably introduced, mainly close to the core, under the influence of the Mo atoms. However, perturbations in the crystallographic order are not exclusively created in this initial process step. In fact, as we observed, the reordering is completed after annealing at 1150°C for 2 h. This means that a much shorter time at the sintering temperature would be sufficient to anneal it. This time can be estimated as follows. The frequency of Mo atomic jumps is of the order of $\nu_D \exp(-E/kT)$, where ν_D and E have the same meanings as above. The annealing time is accordingly $t = (n/\nu_D)\exp(E/kT)$, where n is the number of atomic jumps per Mo atom for reordering (assumed to be small). This equation shows that t_1 and t_2 corresponding to temperatures T_1 and T_2 are related by $T_1 \ln t_1 - T_2 \ln t_2 = (-30 + \ln n)(T_1 - T_2)$. If $t_1 = 7200$ s for $T_1 = 1423$ K, we obtain $t_2 \approx 8$ s for $T_2 = 1723$ K. Thus, the disorder in the inner rim close to the core is necessarily generated or maintained after the end of the sintering process, that is during the cooling after sintering. We propose an explanation for this disorder on the basis of the following cermet properties.

An enrichment of N in cores close to the core–rim boundary was observed in different cermets during cooling after sintering (Zackrisson *et al.* 2000). These authors interpreted this observation as the effect of N, which decreases the solubility of Mo and W in (Ti, Mo, W)(C, N) during cooling. They proposed that this effect does not inhibit the inner rim formation during heating because this step takes place at a moment when the N activity is low, owing to the open porosity during solid-state sintering (Zackrisson *et al.* 2000). However, during cooling, the solubility of N and Mo in (Ti, Mo)(C, N) decreases, forcing either N or Mo atoms to leave the inner rim (Zackrisson *et al.* 2001). As the mobility of N atoms is higher than that of heavy metal atoms, they will diffuse towards the core, as this region is Mo free.

Mo atoms also tend to diffuse, mostly in the sense opposite to that of N, that is towards the outer rim. The mobility of Mo is much lower than that of N, but it can be significant, at least over short distances. Zackrisson *et al.* (2001) reported indeed that the spatial distribution of the different elements (including the heaviest elements) in the inner rim is more homogeneous in a fully sintered material than in a material for which the sintering process was interrupted when the sintering temperature was reached. This demonstrates that Mo atoms can diffuse over short distances at the sintering temperature. This diffusional activity can be at the origin of the strong crystallographic disorder and of the slight increase in lattice parameter in the inner rim next to the core interface. Diffusion results in a high density of defects, including point defects as interstitial atoms. The cooling freezes the disorder in the course of this process.

Once the N concentration has decreased in the inner rim, the driving force that makes Mo atoms diffuse disappears. During subsequent anneals, interstitial atoms can then move to neighbouring vacancy sites, and dislocations can annihilate by climbing, both processes being correlated. The motion of interstitial atoms is the only possibility that accounts for a rapid decrease in the lattice parameter to its equilibrium value, as well as for global reordering, even when only short-range diffusion is allowed. According to this interpretation, the activation energy of annealing is that of defect diffusion.

Thus, through the direct HRTEM observation of the nanometric crystallographic defects in as-sintered samples, and their progressive annealing as a function of the temperature up to 1150°C, our results confirm the hypothesis of Zackrisson *et al*. This process is reminiscent of the damage created in ion-irradiated semiconductors (Werner and Paseman 1982, Sadana *et al*. 1984, Claverie *et al*. 1988, Zheng *et al*. 1991) and alloys (Jaouen *et al*. 1987). Their conventional TEM and HRTEM observations indeed showed that these materials exhibit important decrease in the crystalline order involving lattice distortions, nanosize dislocations, twin nuclei and amorphous zones. This disorder results from the high density of point defects, including interstitial atoms, introduced by the irradiation. To our knowledge, it is the first time that the same kind of disorder has been observed as the result of a chemical instability.

Our results allow us to understand better the high hardness of cermets with a high Mo content at intermediate temperatures. Since these materials have a small grain size the high hardness at intermediate temperatures is (at least partly) the result of the Hall–Petch effect mentioned in the introduction. As confirmed by our observations, the role of Mo in this respect is to reduce the core dissolution during sintering and, consequently, to inhibit the grain growth. In addition, and in agreement with the model of Cutard *et al*. (1996a,b), we also consider the core–rim interface as an efficient obstacle against dislocation movements. Indeed, this effect is clearly observed in figure 3 (a), where the rim contains a higher density of submicrometric dislocations than the core. Then, the disorder close to the interface, which is an increasing function of the Mo content, is thought to be an important contribution to this difficulty and, consequently, of high Mo-content cermets, at least at low enough temperatures to avoid fast reordering.

§ 5. Conclusions

In Mo-containing Ti(C, N)-based cermets, the interfaces between the core and the rim have been analysed as a function of annealing temperature. The analyses show the following.

(i) Mo atoms are concentrated in the rim close to the core–rim interface even after annealing.
(ii) The crystal lattice is heavily distorted in the rim close to the core–rim interface of as-sintered samples (high-Mo-content zones). Distortions correspond to local misorientations, variations in lattice parameter, and dislocations. They progressively disappear upon annealing at 900 and 1150°C.
(iii) No other substructure evolution is observed after annealing.

These results have been interpreted as follows.

(i) It is known that the decrease in the solubility of Mo and W in (Ti, Mo, W)(C, N) induces the diffusion of N atoms into the core during cooling. The observed disorder is then interpreted as the result of the tendency of heavy Mo atoms to diffuse in the opposite direction. The driving force for diffusion ceases when a certain amount of N atoms has penetrated into the core. The disorder can then recover upon subsequent annealing, when atoms can move to neighbouring vacancy sites and dislocations are annihilated.

(ii) The high yield stress of Mo-rich cermets at intermediate temperatures are the result of, firstly, the difficult movement of dislocations across the core–rim interface, due to Mo atoms and lattice defects, and, secondly, the smaller grain size, on account of the Hall–Petch law.

Acknowledgements

The present authors thank Professor W. Benoit, Dr G. Feusier, Dr T. Viatte and Dr D. Caillard for fruitful discussions. They express their gratitude to Stellram-Gland, Switzerland, for providing samples, and Centre Interdépartemental de Microscopie Electronique, Ecole Polytechnique Fédérale de Lausanne for TEM and SEM facilities. The financial support from the Swiss Commission pour la Technologie et l'Innovation (project 32105.1) is gratefully acknowledged.

References

Aigner, K., Lengauer, W., Rafaja, D., and Ettmayer, P., 1994, *J. Alloys Compounds*, **215**, 121.

Claverie, A., Vieu, C., Fauré, J., and Beauvillain, J., 1988, *J. appl. Phys.*, **64**, 4415.

Cutard, T., Viatte, T., Feusier, G., and Benoit, W., 1996b, *Mater. Sci. Engng*, **A209**, 218.

Cutard, T., Bolognini, S., Feusier, G., Viatte, T., and Benoit, W., 1996a, *Proceedings of the European Conference in Powder Metallurgy*: Properties/Testing (Stockholm: European Powder Metallurgy Association), p. 219.

Doi, H., 1986, *Inst. Phys. Conf. Ser.*, **75**, 489.

Feusier, G., 1997, PhD Thesis 1659, Ecole Polytechnique Fédérale de Lausanne, Lausanne, Switzerland, p. 33.

Gee, M. G., Reece, M. J., and Roebuck, B., 1992, *J. Hard Mater.*, **3**, 119.

Hall, E. O., 1951, *Proc. phys. Soc.* B, **64**, 742.

Heuer, A. H., Sears, J. S., and Zaluzec, N. J., 1986, *Inst. Phys. Conf. Ser.*, **75**, 321.

Hitachi 1990, US pat. 4904445.

Humenik, M., and Parikh, N. M., 1956, *J. Am. Ceram. Soc.*, **39**, 60.

Jaouen, C., Ruault, M. O., Bernas, H., Rivière, J. P., and Delafond, J., 1987, *Europhys. Lett.*, **4**, 1031.

Kosolapova, T. Y., 1990, *Handbook of High Temperature Compounds*: *Properties*, *Production*, *Application*, edited by T.Y. Kosolapova (New York: Hemisphere), pp. 323–324.

Mari, D., Bolognini, S., Feusier, G., Viatte, T., and Benoit, W., 1999, *Int. J. Refract. Metals Hard Mater.*, **17**, 209.

Mari, D., Bolognini, S., Feusier, G., Cutard, T., Verdon, C., Viatte, T., and Benoit, W., 2003a, *Int. J. Refract. Metals Hard Mater.*, **21**, 37.

Mari, D., Bolognini, S., Feusier, G., Cutard, T., Viatte, T., and Benoit, W., 2003b, *Int. J. Refract. Metals Hard Mater.*, **21**, 47.

Petch, N. J., 1953, *J. Iron Steel Inst. London*, **174**, 25.

Rolander, U., and Andrén, H.-O., 1988, *Mater. Sci. Engng*, **A105**–**A106**, 283.

Rudy, E., 1976a, US Pat. 3971656; 1976b, US Pat. 3994692.

Sadana, D. K., Sands, T., and Washburn, J., 1984, *Appl. Phys. Lett.*, **44**, 623.

Stadelmann, P. A., 1987, *Ultramicroscopy*, **21**, 131.

van Essen, C. G., 1979, *Electron Microscopy and Microanalysis of Crystalline Materials*, edited by J.A. Belk (Barking, Essex: Applied Science), Chapter 5, pp. 109–110.

Werner, P., and Pasemann, M., 1982, *Ultramicroscopy*, **7**, 267.

Zackrisson, J., Rolander, U., and Andrén, H.-O., 2001, *Metall. Mat. Trans.* A, **32**, 85.

Zackrisson, J., Rolander, U., Jansson B., and Andrén, H.-O., 2000, *Acta mater.*, **48**, 4281.

Zheng, P., Ruault, M. O., Pitaval, M., Descouts, B., Krauz, P., Gasgnier, M., and Crestou, J., 1991, *Appl. Phys. Lett.*, **59**, 1594.